

Methodology of optimisation for a nanostructured two-photon absorption photodetector

Maxence Dauphin

ONERA: Office National d'Etudes et de Recherches Aeronautiques et Spaciales

Baptiste Fix (✉ baptiste.fix@onera.fr)

ONERA: Office National d'Etudes et de Recherches Aeronautiques et Spaciales <https://orcid.org/0000-0002-5610-9078>

Julien Jaeck

ONERA: Office National d'Etudes et de Recherches Aeronautiques et Spaciales

Riad Haïdar

ONERA: Office National d'Etudes et de Recherches Aeronautiques et Spaciales

Research

Keywords: Two-photon absorption, Nanostructures, Infrared photodetection

Posted Date: May 17th, 2021

DOI: <https://doi.org/10.21203/rs.3.rs-492917/v1>

License: © ⓘ This work is licensed under a Creative Commons Attribution 4.0 International License.

[Read Full License](#)

RESEARCH

Methodology of optimisation for a nanostructured two-photon absorption photodetector

Maxence Dauphin¹, Baptiste Fix^{1*}, Julien Jaeck¹ and Riad Haïdar^{1,2}

*Correspondence:

baptiste.fix@onera.fr

¹DOTA, ONERA, Université Paris-Saclay, 91123 Palaiseau, France

Full list of author information is available at the end of the article

Abstract

We introduce a 3-step method to optimise a nanostructured photodetector for infrared sensing through non degenerated two-photon absorption (NDTPA). First, the nanostructure is designed to tailor the distribution and concentration of both pump and signal intensities within the absorbing layer, thus leading to a gain in two-photon absorption. Second, the issue of the competition between NDTPA and other sub-bandgap transitions is tackled with a new figure of merit to favor as much as possible NDTPA while minimising other absorption processes. Third, a refined computation of the gain and the figure of merit is done to consider focused beams. Finally, two scenarios based on low power infrared photodetection are investigated to illustrate the flexibility and adaptability of the method. It is shown that the gain is up to 7 times higher and the figure of merit is up to 20 times higher compared to the literature.

Keywords: Two-photon absorption; Nanostructures; Infrared photodetection

Introduction

Quantum infrared photodetection is classically done through direct absorption of a photon to enable an electronic transition in so-called linear light sensors. Several photodetection technologies are currently in competition in the mid-wave (3-5 μm) and long-wave (7-12 μm) infrared spectrum such as the bulk semiconductor technologies HgCdTe [1] and InSb [2], the quantum-well structures (QWIP) [3, 4, 5], or the type II super-lattices (T2SL) [6, 7]. Yet, owing to the small energy of infrared photons and thus of the electronic transition, background limited performances (BLIP) are only achieved at cryogenic temperature. The needed cooling machine limits the operability and the mean time before failure of the infrared photodetectors.

In parallel to the race toward higher operating temperature (HOT) of linear light sensors [8], new photodetection paradigm using non-linearities have been proposed either at the second [9] or third order processes [10, 11, 12]. Among these third order phenomenon, two-photon absorption in higher band-gap energy semiconductors presents interesting properties for room temperature infrared photodetection. It consists in the quasi-simultaneous absorption of two photons [13] which makes it naturally interesting for high frequency and heterodyne application [10, 11]. However, the low quantum efficiency of the mechanism [14] remains a strong limitation.

In order to tackle this issue, the nanostructures have been used for photon-harvesting [15], photon-trapping (MIM [16], GMR [17], etc.) and to locally enhance the electrical field [18]. In the case of infrared photodetection, these properties have

proven to enhance sensing performances [19, 20, 21], mainly thanks to the reduction of the absorbing semiconductor volume. As well, the low efficiency of two-photon absorption can be improved thanks to the concentration ability of nanostructures [12] - even in the challenging case of bi-spectral optimisation. Indeed, an adapted nanostructuration makes it possible to concentrate and colocalise each beam intensities, leading to a gain and consequently to greater photogenerated currents [22].

Discussion

In this paper, we describe our methodology to optimise two-photon infrared photodetection in nanostructured detectors. First, we explain and quantify how nanostructures can enhance two-photon absorption (especially non-degenerated two-photon absorption called NDTPA) through fields concentration and colocalisation. Then, the competition between NDTPA and other sub-bandgap transitions is discussed, leading to the definition of a figure of merit for the design of the diodes. This figure of merit is then refined to tackle the issue of focused optical beams. Finally, the figure of merit is adapted to address a selection of low power infrared applications, namely monochromatic photodetection and infrared imaging.

Two photon infrared photodetection has been previously discussed in the literature [12, 22, 23, 24] with reasonable success. Yet, up to now the low responsivity and signal-to-noise ratio (SNR) have limited this technology to either short-pulsed laser sources or elaborated lab experiments. Based on one of these most recent works [22], we will revisit the optimisation process of a nanostructured detector design in order to take full benefit of the nanostructures for low power infrared photodetection. We will focus on the absorption process ; the transport and carrier collection will not be covered. The concepts discussed here will thus be illustrated on the photodiode characterised in [22], numerically simulated by the linear B-Spline modal method [25]. As illustrated in Figure 1, the photodetector is a PIN diode made of Indium Phosphide (InP). Since the structure is supposed infinite along the y -direction and infinitely periodic along the x -direction, the computation can be reduced to the PIN area $L = d * h$. InP is known to be transparent in the infrared spectrum (bandgap energy $E_g = 1.344$ eV [26, 27]) and to exhibit a high third order non-linear susceptibility [28]. For the simplicity and generalisation of the discussion, the doped region of the PIN junction will not be taken into account. Thus the absorbing layer is numerically defined as an unified optical index. The InP allows to absorb simultaneously a $3.39 \mu\text{m}$ signal photon ($\hbar\omega_s = 0.36$ eV) with a $1.06 \mu\text{m}$ pump photon ($\hbar\omega_p = 1.17$ eV) since $\hbar\omega_s + \hbar\omega_p \geq E_g$. This leads to a local carrier generation within the material, which will be swept out by the applied electric field and may participate to the two-photon photocurrent, which writes as :

$$j_{\text{NDTPA}} \sim \beta(\omega_p, \omega_s) i_p i_s \quad (1)$$

with β the two-photon absorption coefficient [13], i_p the local pump intensity, and i_s the local signal intensity.

Nanostructured electrodes are used to tailor both the concentration and colocalisation of the two intensities inside the diode. Then, under the pump power non

depletion hypothesis, the total current generated through NDTPA in the surface of the absorbing layer is :

$$J_{\text{NDTPA}} = \int_L j_{\text{NDTPA}} dS \sim G \beta(\omega_p, \omega_s) P_p^{(i)} P_s^{(i)} \quad (2)$$

with $P_p^{(i)}$ and $P_s^{(i)}$ incident pump and signal power over one period, L the area of the absorbing region.

Finally, G is the dimensionless nanostructure gain which is formulated as :

$$G = \int_L \frac{i_p(x, y) i_s(x, y)}{P_p^{(i)} P_s^{(i)}} dS = \int_L I_p I_s dS \quad \text{with} \quad I_p = \frac{i_p}{P_p^{(i)}} \quad \text{and} \quad I_s = \frac{i_s}{P_s^{(i)}} \quad (3)$$

The intensity map on Figure 1.c illustrates the capability of the nanostructure to concentrate and colocalise the intensities I_p and I_s , thus increasing the TPA by a gain $G = 120$ for the optimal optical configuration (a collimated TE polarised $3.39 \mu\text{m}$ signal at normal incidence and a collimated TE-polarised pump at $1.06 \mu\text{m}$ pump with an angle of incidence of 11.83°). However, other pump related sub-bandgap processes have been shown to compete with NDTPA [29, 30, 31], leading to a higher background current and thus a lower SNR especially for low signal intensity.

The total carrier generation given in equation 4 is made of three contributions. The first one comes from the NDTPA. The second term is the degenerated two-photon absorption (DTPA) of the pump. The third term is the phenomenon called Photon Assisted Shockley-Read-Hall effect (PASRH) [30], corresponding to a two step transition : the absorption of a pump photon into or from a sub-gap energy level induced by the material defects completed by a thermally activated transition. This PASRH is proportional to the pump intensity but the linear coefficient depends on a thermal absorption with many traps involved leading to complex predictions.

$$J_{\text{total}} \propto \left(\beta(\omega_p, \omega_s) \int_L I_p I_s dS + \beta(\omega_p, \omega_p) \int_L I_p^2 dS + \alpha(\omega_p) \int_L I_p dS \right) P_p^{(i)} P_s^{(i)} \quad (4)$$

A direct comparison of these three terms is difficult. Yet, some broad considerations can be made. First, a complete computation of β [32] is illustrated in Figure 2.b and the two TPA processes (NDTPA and DTPA) are underlined. Since β gets higher away from degeneracy (i.e. $\omega_p \gg \omega_s$), the NDTPA is favored.

Unfortunately, the PASRH also increases with the pump photon energy [29], thus a balance has to be found to increase the NDTPA while limiting the PASRH. In our configuration, $\beta_{\text{NDTPA}} = 87 \text{ cm.GW}^{-1}$ is almost four times greater than $\beta_{\text{DTPA}} = 24 \text{ cm.GW}^{-1}$ while the pump energy represents 87% of the gap energy.

Since the structure should favor the NDTPA, the term $\int_L I_p I_s$ needs to be as high as possible. At the same time, the terms $\int_L I_p^2$ and $\int_L I_p$ must be as low as possible to limit the DTPA and PASRH. To illustrate this concept, the normalised

pump intensity and signal intensity maps have been depicted on figure 3.a and 3.b. These maps illustrate the intensity distribution inside the structure and are thus related to the absorption processes that are possible at the various positions. Most importantly, the signal intensity map illustrates the location where NDTPA could happen and should be maximised. However the pump intensity map is more difficult to interpret. Indeed, while the pump intensity is needed to activate NDTPA, it also gives way to the competitive DTPA and PASRH processes. So we suggest to differentiate the "useful" pump intensity that contributes to NDTPA from the rest. This leads to the definition of the area \mathcal{A} where I_s is below a threshold that we arbitrary fix at 20% of its maximum (see figure 3.a). We consider that the pump intensity located inside \mathcal{A} cannot contribute to NDTPA and should be minimised. Conversely, the pump intensity located outside \mathcal{A} can be interpreted as useful for NDTPA and has to be maximised (see figure 3.c). The fraction of I_p inside \mathcal{A} which is detrimental to efficient photodetection through NDTPA is illustrated in figure 3.d.

While only the gain G (see equation 3) was previously investigated in the literature to optimise the nanostructures due to its direct relation to NDTPA, we propose here to refine the optimisation process to tackle the issue of the pump distribution. A new figure of merit, called F , is built as the ratio of NDTPA over the avoidable DTPA and PASRH.

$$F = \frac{\int_{\mathcal{L}} \tilde{I}_p I_s dS}{\int_{\mathcal{L}} \tilde{I}_p^2 dS \int_{\mathcal{A}} \tilde{I}_p dS} \quad \text{with} \quad \int_{\mathcal{L}} \tilde{I}_p dS = 1 \quad (5)$$

\tilde{I}_p is the normalised pump intensity in the layer that enables the comparison between very different structures if one assumes the non-depletion of the pump power.

Furthermore a complementary optimisation is needed for infrared detection through NDTPA. Indeed, the optical beam is usually focused onto the detector. On the other hand the nanocavities resonances are known to spectral shift with the angle of incidence. As the figure 4 illustrates, the structure was optimised for a collimated pump with an incidence angle of $\theta_p^i = 11.83^\circ$ and a collimated signal at normal incidence. The best configuration leads to a gain up to $G = 120$ and a figure of merit up to $F = 140 \text{ cm}^{-1}$. However, the gain and the figure of merit drop can be drastic with a modification of any one of the incident angles.

One can simulate the effect of a focused beam as the pondered mean of F and G over the cone of incidence angles - this is expected to greatly reduce both the gain and the figure of merit. Effectively, as the figure 4.c and 4.d illustrate both G and F drop for a focused pump beam (cone of half-angle $\varphi_p = 2^\circ$). This observation brings the need for a refined optimisation procedure, which is driven by the aimed application of the photodetector.

We now propose to make use of our 3-step optimisation : maximisation of gain G (NDTPA enhancement), maximisation of figure of merit F (sub-gap competition) and optimisation of angular tolerance (use of focused beams), in the configuration

where a signal beam (around $3.39 \mu\text{m}$) and a pump beam ($1.06 \mu\text{m}$) are both focused on a photodiode. The methodology introduced here is still suitable to any infrared wavelength, according to the desired function. And thanks to the generality of this methodology, one can straightforwardly adapt the optimisation process to another specific application. To illustrate the flexibility of our optimisation methodology, two structures tackling different infrared photodetection scenarios are introduced.

The first structure is a nanostructured InP junction absorbing at $3.41 \mu\text{m}$ (see Figure 5.a) for monochromatic LIDAR or heterodyne detection. We emphasize that, for this application, the spectral absorption bandwidth is not a relevant feature. Moreover, since heterodyne detection tends to operate with large pixels, the signal will not be strongly focused and the angular stability of G or F is not a crucial feature. Based on these principles, a guided mode is used for the signal concentration. This resonance seems well suited since, despite a low angular stability, it allows a field concentration that spreads over a large area of the junction. The pump resonance is based on a vertical Fabry-Perot which displays an interesting angular stability. More details on the optimised structure are available in the supplementary materials. As illustrated on Figure 5 and Table 1, the optimised structure presents, for a focused pump with a 2° half-cone angle, a gain $G = 35$ and a figure of merit $F = 108 \text{ cm}^{-1}$ that are respectively 7 and 5 times higher than those of the literature. The angular stability of G and F is about 3° which is coherent with the application. In addition, it is noteworthy that, contrary to the structure from literature, both pump and signal are working at normal incidence which highly simplifies the use of such photodetectors.

The second structure is a nanostructured gallium arsenide (GaAs) junction with an extended absorption band in the MWIR ($3\text{-}4 \mu\text{m}$) for imaging applications. In this regard, the device requires both a wide spectral absorption band and an angular stability at least up to 10° . To this end a coupled nano-Fabry Perot (nFPc) [33] resonator is used for the signal concentration. The nFPc enables to design several resonances with similar field distribution and high angular tolerance. More details on the optimised structure are available in the supplementary materials. As illustrated on Figure 5 and Table 1, the angular mean values of $G(3.39 \mu\text{m}) = 10.6$ and $G(3.66 \mu\text{m}) = 12.6$ are about 4 times higher than the angular mean value of the literature $G = 2.88$ [22]. As expected, the increased spectral bandwidth and the angular stability come at the cost of 3 times lower gain at normal incidence as compared to the one of the monochromatic structure. With regards of the figure of merit, the introduction of a multispectral nanostructure imposes to redefine the detrimental pump intensity. Indeed, the pump intensity that is colocalised with either signal intensity can enable NDTPA. Thus the area \mathcal{A} has to be defined with regards to each signal resonance such as : $\mathcal{A} = \mathcal{A}_{3.39 \mu\text{m}} \cup \mathcal{A}_{3.66 \mu\text{m}}$. Finally, the figure of merit F is almost constant with regard to the signal half-cone angle which is relevant with the expectations.

Thus two structures with distinct objectives have been depicted, based on an optimisation process through the figure of merit design. Consequently the resonator choice is made to meet the device requirements. Many configurations may be possible for the desired application but the figure of merit sets up points of comparison

for every case. Therefore this methodology is flexible and suitable for various devices and tunable for various spectral configurations.

Conclusion

In conclusion, a methodology to optimise two-photon photodetection in nanostructured detectors for low power infrared sensors was described. Based on the NDTPA equations and its competition with two other sub-bandgap absorption processes, we suggested a 3-step optimisation procedure. First comes the structure gain, which quantifies NDTPA through the colocalisation of the pump and the signal intensities. Second the ratio of NDTPA over the avoidable DTPA and PASRH that can be interpreted as a signal to noise optimisation. And third comes the structure angular tolerance, which is required for most applications where the optical beams are focused. As a result, the optimisation methodology was demonstrated for two structures aiming at distinct scenarios. This optimisation methodology can easily be adapted to various wavelenghtes, various absorbing junction and various applications ; it paves the way to new efficient designs.

Acknowledgements

This work was supported by a DGA-AID scholarship.

Funding

Office National d'études et de Recherches Aérospatiales ; Direction Générale de l'Armement.

Disclosures

The authors declare no conflicts of interest.

Author details

¹DOTA, ONERA, Université Paris-Saclay, 91123 Palaiseau, France. ²École Polytechnique, Département de Physique, 91128 Palaiseau, France.

References

- Rogalski, A.: HgCdTe photodetectors. In: Tournié, E., Cerutti, L. (eds.) Mid-infrared Optoelectronics. Woodhead Publishing Series in Electronic and Optical Materials, pp. 235–335. Woodhead Publishing, ??? (2020). doi:10.1016/B978-0-08-102709-7.00007-3. <https://www.sciencedirect.com/science/article/pii/B9780081027097000073> Accessed 2021-04-19
- Klipstein, P., Aronov, D., Ezra, M.b., Barkai, I., Berkowicz, E., Brumer, M., Fraenkel, R., Glzman, A., Grossman, S., Jacobsohn, E., Klin, O., Lukomsky, I., Shkedy, L., Shtrichman, I., Snapi, N., Yassen, M., Weiss, E.: Recent progress in InSb based quantum detectors in Israel. *Infrared Physics & Technology* **59**, 172–181 (2013). doi:10.1016/j.infrared.2012.12.035. Accessed 2021-04-20
- Rogalski, A.: Quantum well photoconductors in infrared detector technology. *Journal of Applied Physics* **93**, 4355–4391 (2003). doi:10.1063/1.1558224
- Choi, K.K., Jhabvala, M.D., Sun, J., Jhabvala, C.A., Waczynski, A., Olver, K.: Resonator-quantum well infrared photodetectors. *Applied Physics Letters* **103**(20), 201113 (2013). doi:10.1063/1.4831797. Publisher: American Institute of Physics. Accessed 2021-04-20
- Ivanov, R., Smuk, S., Hellström, S., Evans, D., Höglund, L., Costard, E.: LWIR QWIPs at IRnova for next generation polarimetric imaging. *Infrared Physics & Technology* **95** (2018). doi:10.1016/j.infrared.2018.10.017
- Rogalski, A., Kopytko, M., Martyniuk, P.: InAs/GaSb type-II superlattice infrared detectors: three decades of development, p. 1017715 (2017). doi:10.1117/12.2272817
- Rogalski, A., Martyniuk, P., Kopytko, M.: Type-II superlattice photodetectors versus HgCdTe photodiodes. *Progress in Quantum Electronics* **68**, 100228 (2019). doi:10.1016/j.pquantelec.2019.100228. Accessed 2021-04-19
- Rogalski, A., Martyniuk, P., Kopytko, M., Hu, W.: Trends in Performance Limits of the HOT Infrared Photodetectors. *Applied Sciences* **11**(2), 501 (2021). doi:10.3390/app11020501. Accessed 2021-03-08
- Langrock, C., Diamanti, E., Roussev, R.V., Yamamoto, Y., Fejer, M.M., Takesue, H.: Highly efficient single-photon detection at communication wavelengths by use of upconversion in reverse-proton-exchanged periodically poled LiNbO₃ waveguides. *Optics Letters* **30**(13), 1725–1727 (2005). doi:10.1364/OL.30.001725. Publisher: Optical Society of America. Accessed 2021-03-22
- Boitier, F., Godard, A., Rosencher, E., Fabre, C.: Measuring photon bunching at ultrashort timescale by two-photon absorption in semiconductors. *Nature Physics* **5**(4), 267–270 (2009). doi:10.1038/nphys1218. Number: 4 Publisher: Nature Publishing Group. Accessed 2021-01-14
- Fishman, D.A., Cirloganu, C.M., Webster, S., Padilha, L.A., Monroe, M., Hagan, D.J., Van Stryland, E.W.: Sensitive mid-infrared detection in wide-bandgap semiconductors using extreme non-degenerate two-photon absorption. *Nature Photonics* **5**(9), 561–565 (2011). doi:10.1038/nphoton.2011.168. Number: 9 Publisher: Nature Publishing Group. Accessed 2021-03-19

12. Portier, B., Vest, B., Pardo, F., Péré-Laperne, N., Steveler, E., Jaeck, J., Dupuis, C., Bardou, N., Lemaître, A., Rosencher, E., Haïdar, R., Pelouard, J.-L.: Resonant metallic nanostructure for enhanced two-photon absorption in a thin GaAs p-i-n diode. *Applied Physics Letters* **105**(1), 011108 (2014). doi:10.1063/1.4887375. Publisher: American Institute of Physics. Accessed 2021-01-14
13. Hutchings, D.C., Stryland, E.W.V.: Nondegenerate two-photon absorption in zinc blende semiconductors. *JOSA B* **9**(11), 2065–2074 (1992). doi:10.1364/JOSAB.9.002065. Publisher: Optical Society of America. Accessed 2021-03-10
14. Stryland, E.W.V., Woodall, M.A., Vanherzeele, H., Soileau, M.J.: Energy band-gap dependence of two-photon absorption. *Optics Letters* **10**(10), 490–492 (1985). doi:10.1364/OL.10.000490. Publisher: Optical Society of America. Accessed 2021-03-09
15. Nga Chen, Y., Todorov, Y., Askenazi, B., Vasanelli, A., Biasiol, G., Colombelli, R., Sirtori, C.: Antenna-coupled microcavities for enhanced infrared photo-detection. *Applied Physics Letters* **104**(3), 031113 (2014). doi:10.1063/1.4862750. Accessed 2021-03-09
16. Koechlin, C., Bouchon, P., Pardo, F., Pelouard, J.-L., Haïdar, R.: Analytical description of subwavelength plasmonic MIM resonators and of their combination. *Optics Express* **21**(6), 7025 (2013). doi:10.1364/OE.21.007025. Accessed 2021-01-04
17. Verdun, M., Portier, B., Jaworowicz, K., Jaeck, J., Lelarge, F., Guilet, S., Dupuis, C., Haïdar, R., Pardo, F., Pelouard, J.-L.: Guided-mode resonator for thin InGaAs P-i-N short-wave infrared photo-diode. *Applied Physics Letters* **108**(5), 053501 (2016). doi:10.1063/1.4941297. Accessed 2021-03-09
18. Fabas, A., El Ouazzani, H., Hugonin, J.-P., Haïdar, R., Greffet, J.-J., Bouchon, P.: Helmholtz-like Nanoresonators Applied to Surface Enhanced Infrared Absorption. In: *Metamaterials 2019, ROME, Italy* (2019). <https://hal.archives-ouvertes.fr/hal-02409551> Accessed 2021-04-29
19. Palaferri, D., Todorov, Y., Bigioli, A., Mottaghizadeh, A., Gacemi, D., Calabrese, A., Vasanelli, A., Li, L., Davies, A.G., Linfield, E.H., Kapsalidis, F., Beck, M., Faist, J., Sirtori, C.: Room-temperature nine- μm -wavelength photodetectors and GHz-frequency heterodyne receivers. *Nature* **556**(7699), 85–88 (2018). doi:10.1038/nature25790. Accessed 2021-03-09
20. Miyazaki, H.T., Mano, T., Kasaya, T., Osato, H., Watanabe, K., Sugimoto, Y., Kawazu, T., Arai, Y., Shigetou, A., Ochiai, T., Jimba, Y., Miyazaki, H.: Synchronously wired infrared antennas for resonant single-quantum-well photodetection up to room temperature, 10 (2020)
21. Haki, M., Lin, Q., Lepillet, S., Billet, M., Lampin, J.-F., Pirotta, S., Colombelli, R., Wan, W., Cao, J.C., Li, H., Peytavit, E., Barbieri, S.: Ultrafast Quantum-Well Photodetectors Operating at 10 μm with a Flat Frequency Response up to 70 GHz at Room Temperature. *ACS Photonics* **8**(2), 464–471 (2021). doi:10.1021/acsp Photonics.0c01299. Publisher: American Chemical Society. Accessed 2021-03-09
22. Fix, B., Jaeck, J., Vest, B., Verdun, M., Beaudoin, G., Sagnes, I., Pelouard, J.-L., Haïdar, R.: Nanostructured diode for infrared photodetection through nondegenerate two-photon absorption. *Applied Physics Letters* **111**(4), 041102 (2017). doi:10.1063/1.4996369. Accessed 2021-02-04
23. Xu, G., Ren, X., Miao, Q., Yan, M., Pan, H., Chen, X., Wu, G., Wu, E.: Sensitive Infrared Photon Counting Detection by Nondegenerate Two-Photon Absorption in Si APD. *IEEE Photonics Technology Letters* **31**(24), 1944–1947 (2019). doi:10.1109/LPT.2019.2950542. Conference Name: IEEE Photonics Technology Letters
24. Fang, J., Wang, Y., Yan, M., Wu, E., Huang, K., Zeng, H.: Highly Sensitive Detection of Infrared Photons by Nondegenerate Two-Photon Absorption Under Midinfrared Pumping. *Physical Review Applied* **14**(6), 064035 (2020). doi:10.1103/PhysRevApplied.14.064035. Accessed 2021-03-09
25. Bouchon, P., Pardo, F., Haïdar, R., Pelouard, J.-L.: Fast modal method for subwavelength gratings based on B-spline formulation. *Journal of the Optical Society of America A* **27**(4), 696 (2010). doi:10.1364/JOSAA.27.000696. Accessed 2021-03-03
26. Levinshtein, M., Rumyantsev, S., Shur, M.: *Handbook Series on Semiconductor Parameters: Volume 1: Si, Ge, C (Diamond), GaAs, GaP, GaSb, InAs, InP, InSb vol. 1.* WORLD SCIENTIFIC, ??? (1996). doi:10.1142/2046-vol1. <https://www.worldscientific.com/worldscibooks/10.1142/2046-vol1> Accessed 2021-03-12
27. Vavilov, V.S.: *Handbook on the physical properties of Ge, Si, GaAs and InP* by A Dargys and J Kundrotas. *Physics-Uspeski* **39**(7), 757–757 (1996). doi:10.1070/PU1996v039n07ABEH001526. Accessed 2021-03-12
28. Nayak, S.K., Sahu, T., Mohanty, S.P.: Third-order nonlinear optical susceptibilities of group IV and III–V compound semiconductors. *Physica B: Condensed Matter* **191**(3), 334–340 (1993). doi:10.1016/0921-4526(93)90093-L. Accessed 2021-04-20
29. Vest, B., Fix, B., Jaeck, J., Haïdar, R.: Competition between sub-bandgap linear detection and degenerate two-photon absorption in gallium arsenide photodiodes. *Journal of the European Optical Society-Rapid Publications* **12**(1), 26 (2016). doi:10.1186/s41476-016-0022-8. Accessed 2021-02-04
30. Vest, B., Lucas, E., Jaeck, J., Haïdar, R., Rosencher, E.: Silicon sub-bandgap photon linear detection in two-photon experiments: A photo-assisted Shockley-Read-Hall mechanism. *Applied Physics Letters* **102**(3), 031105 (2013). doi:10.1063/1.4788705. Publisher: American Institute of Physics. Accessed 2021-01-14
31. Piccardo, M., Rubin, N.A., Meadowcroft, L., Chevalier, P., Yuan, H., Kimchi, J., Capasso, F.: Mid-infrared two-photon absorption in an extended-wavelength InGaAs photodetector. *Applied Physics Letters* **112**(4), 041106 (2018). doi:10.1063/1.5018619. Accessed 2021-03-09
32. Cirloganu, C.M., Padilha, L.A., Fishman, D.A., Webster, S., Hagan, D.J., Stryland, E.W.V.: Extremely nondegenerate two-photon absorption in direct-gap semiconductors [Invited]. *Optics Express* **19**(23), 22951–22960 (2011). doi:10.1364/OE.19.022951. Publisher: Optical Society of America. Accessed 2021-03-10
33. Fix, B., Jaeck, J., Bouchon, P., Héron, S., Vest, B., Haïdar, R.: High-quality-factor double Fabry-Perot plasmonic nanoresonator. *Optics Letters* **42**(24), 5062–5065 (2017). doi:10.1364/OL.42.005062. Publisher: Optical Society of America. Accessed 2021-03-22

Figures
Tables

Figure 1 (a). Scheme of NDTPA in a direct bandgap semiconductor. (b). Drawing of a published nanostructured photodiode designed for infrared photodetection [22] (c). Intensity map of signal and pump colocalisation.

Figure 2 (a). Illustration of the three competitive sub-bandgap absorption processes (NDTPA, DTPA and PASRH). (b). Evolution of the two-photon absorption coefficient of InP with regards to the signal and pump energy.

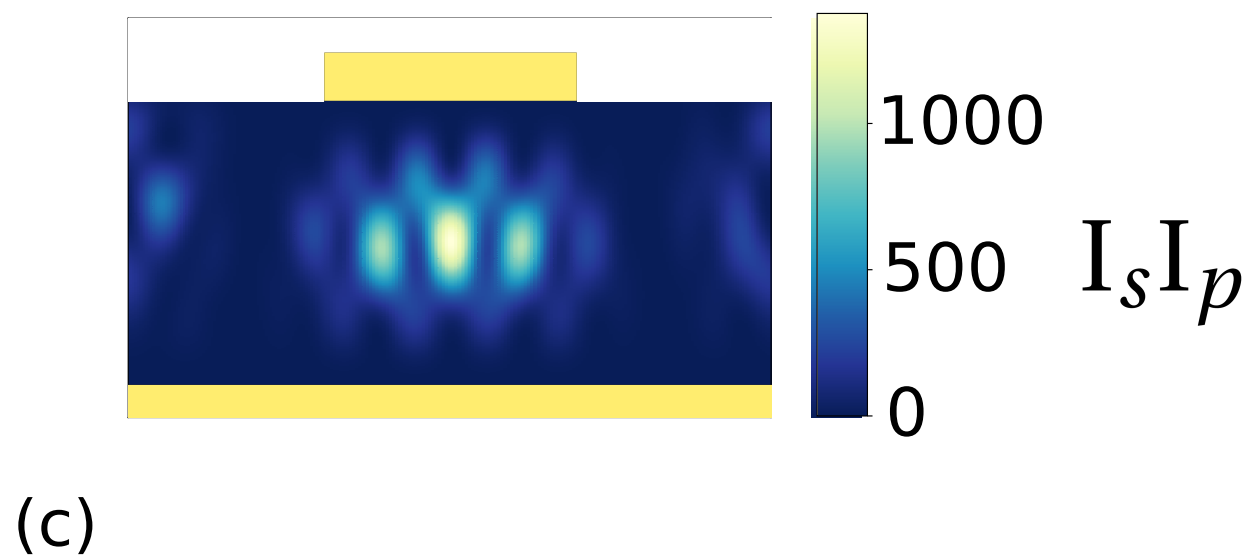
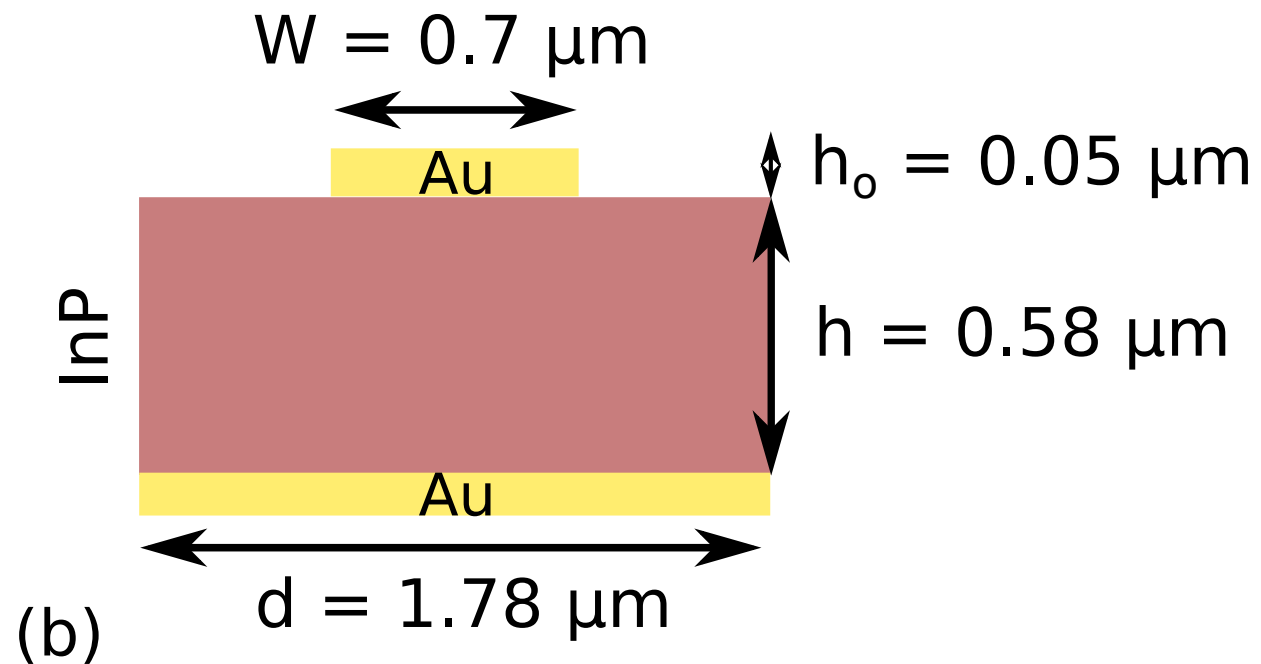
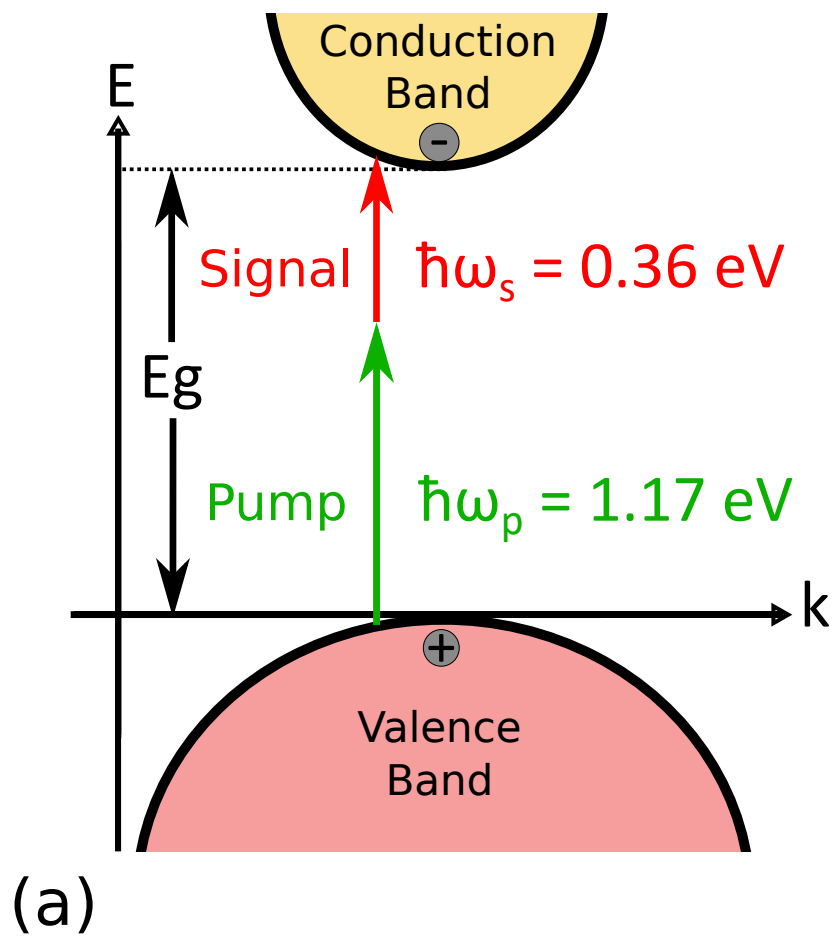
Figure 3 (a). Signal intensity map. A white dotted isoline delimits the surface \mathcal{A} where $I_s < 20\% I_s^{\max}$. (b). Pump intensity map (c). Intensity maps of the signal and pump colocalisation. NDTPA is mostly generated in this area. (d). Pump intensity map in \mathcal{A} . This pump intensity is detrimental since it mainly generates PASRH.

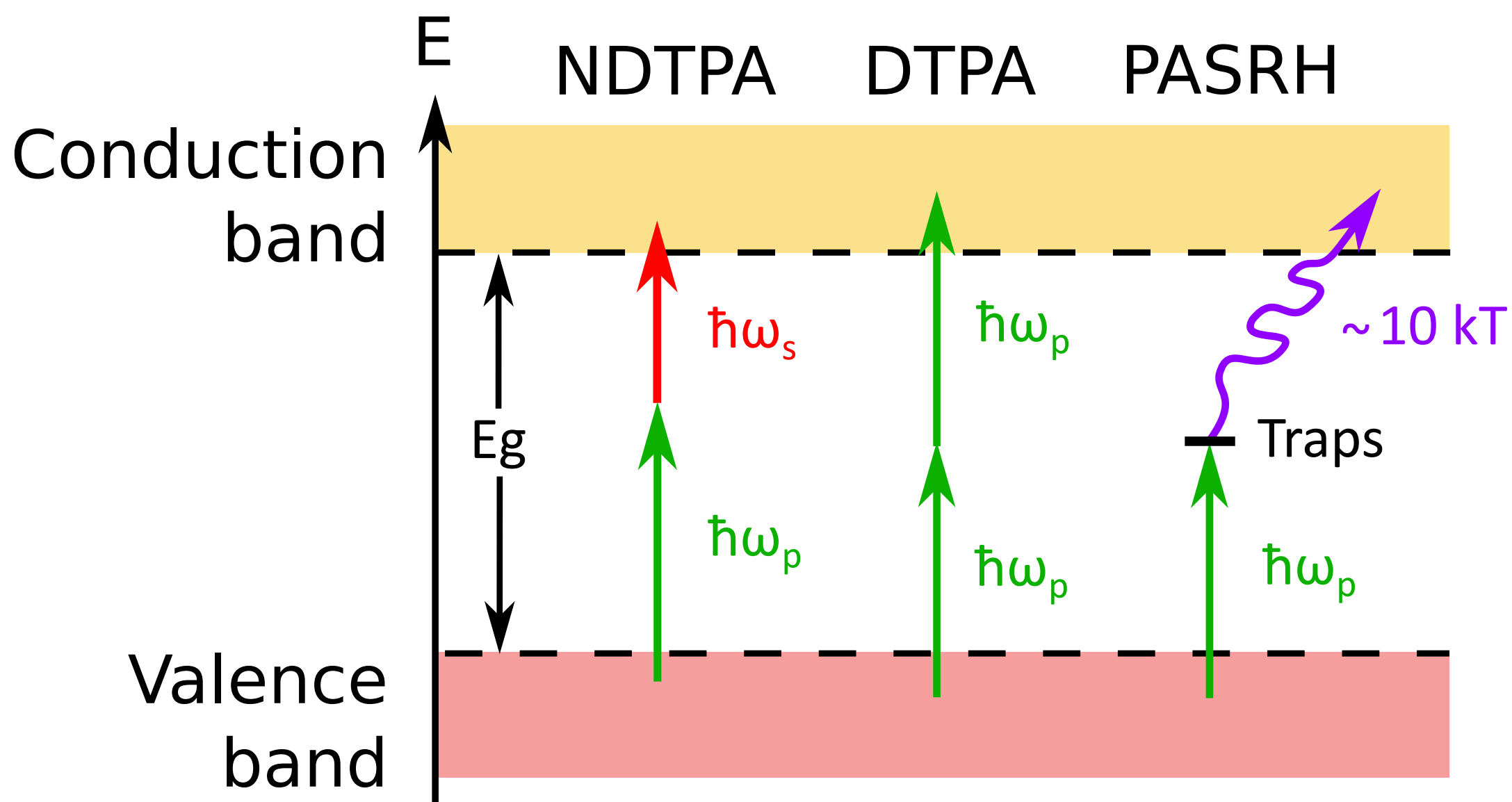
Figure 4 G (a) and F (b) for different incidence signal and pump angles. Both figures depict the best configurations for the detection. The calculation were performed for collimated beams. This structure needs a pump angle of $\theta_p^i = 11.83^\circ$ to detect infrared light. The gaussian ponderated integration of G and F inside the rectangle leads to their focused value. Evolution of G (c) and F (d) values for a focused configuration with the signal half-cone angle φ_s and a fixed pump half-cone angle of $\varphi_p = 2.0^\circ$.

Figure 5 (a). Spectral distribution of the signal intensity of the monochromatic structure ($d_m = 1.21 \mu\text{m}$, $w_m = 0.34 \mu\text{m}$, $h_m = 0.388 \mu\text{m}$ and $h_0 = 0.05 \mu\text{m}$). (b). Spectral distribution of the signal intensity of the bichromatic structure ($d_b = 1.64 \mu\text{m}$, $w_{b_1} = 0.29 \mu\text{m}$, $w_{b_2} = 0.25 \mu\text{m}$, $w_{b_3} = 0.21 \mu\text{m}$, $h_b = 0.190 \mu\text{m}$ and $h_0 = 0.05 \mu\text{m}$). Evolution of G (c) and F (d) values under a focused configuration. The pump is at a fixed wavelength $1.06 \mu\text{m}$, and focused with a half-cone angle of 2° .

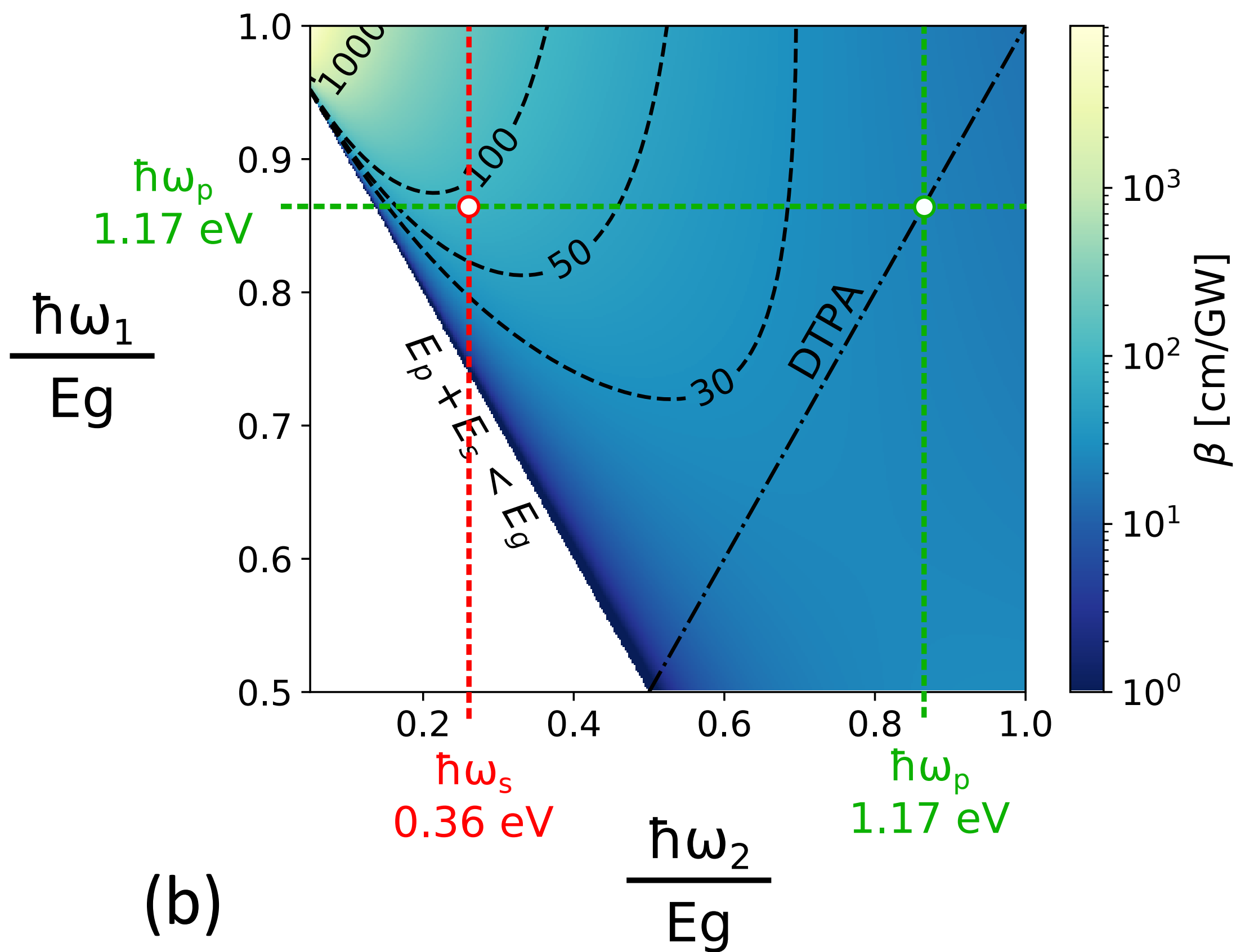
Structure	Signal resonator	Pump resonator	G(0°)	G(10°)	F(0°) [cm ⁻¹]	F(10°) [cm ⁻¹]
Literature [22]	Diffraction order	GMR	4.60	1.20	20.2	5.24
Monochromatic	Guided mode	Vertical Fabry-Perot	35.2	16.3	108	50.0
Bichromatic (3.39 μm)	nFPc	GMR	13.5	10.7	411	325
Bichromatic (3.66 μm)	nFPc	GMR	11.3	10.1	416	373

Table 1 Gain G and figure of merit F values depicted for all the structures. The computation is performed for a focused pump with a half-cone angle of 2° . The signal is either collimated (0°) or focused with a half-cone angle of 10° .



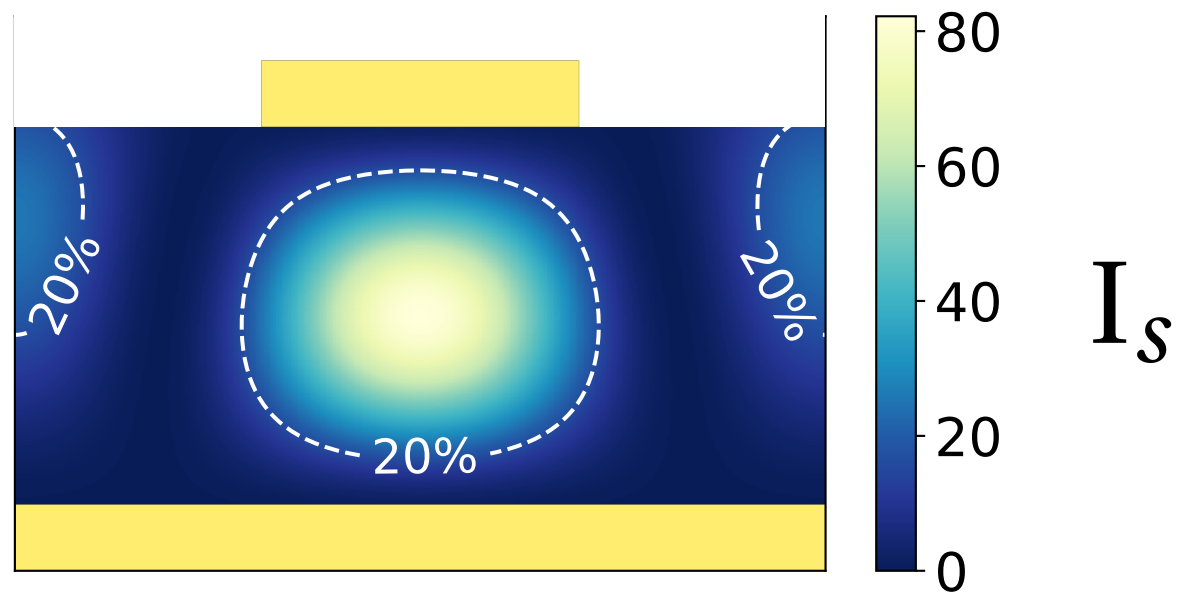


(a)

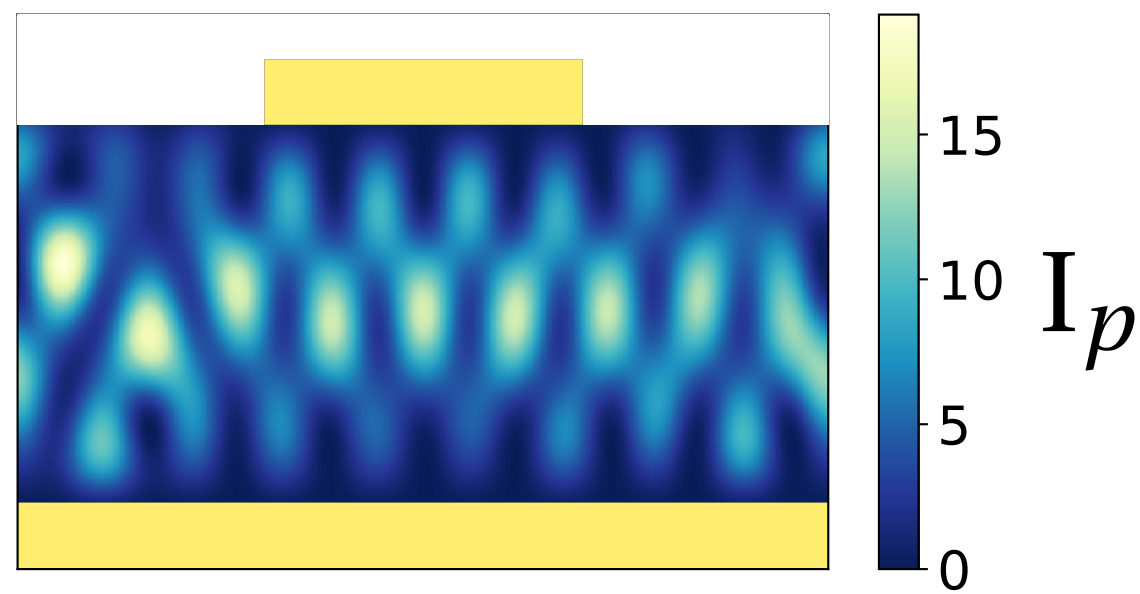


(b)

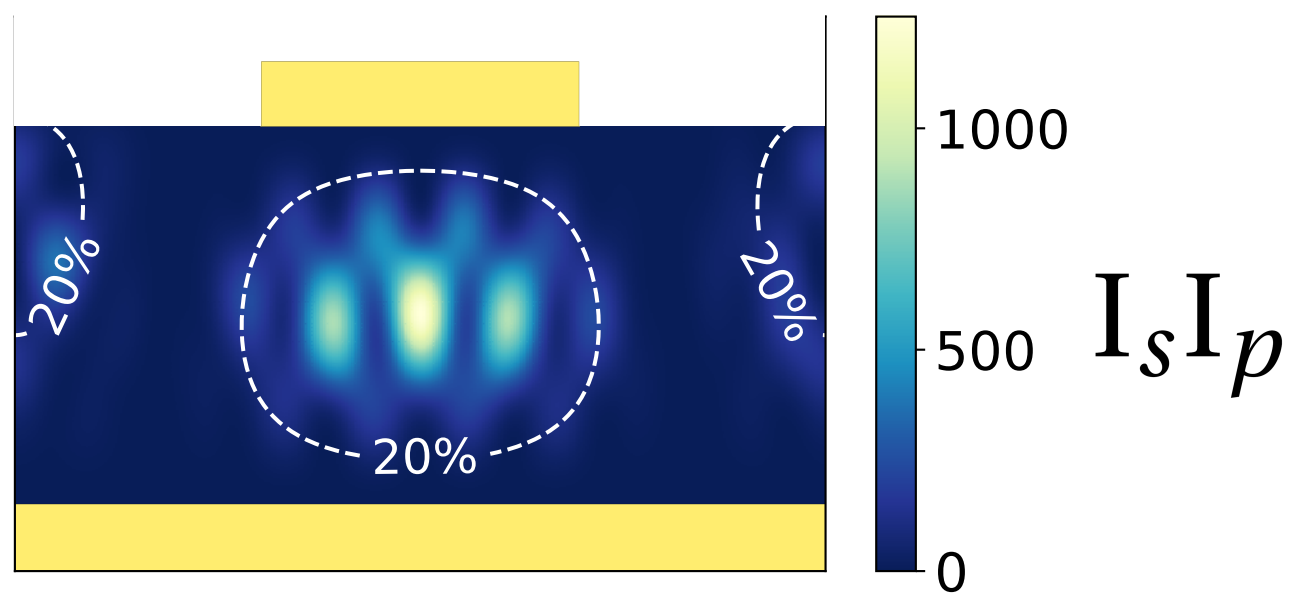
(a)



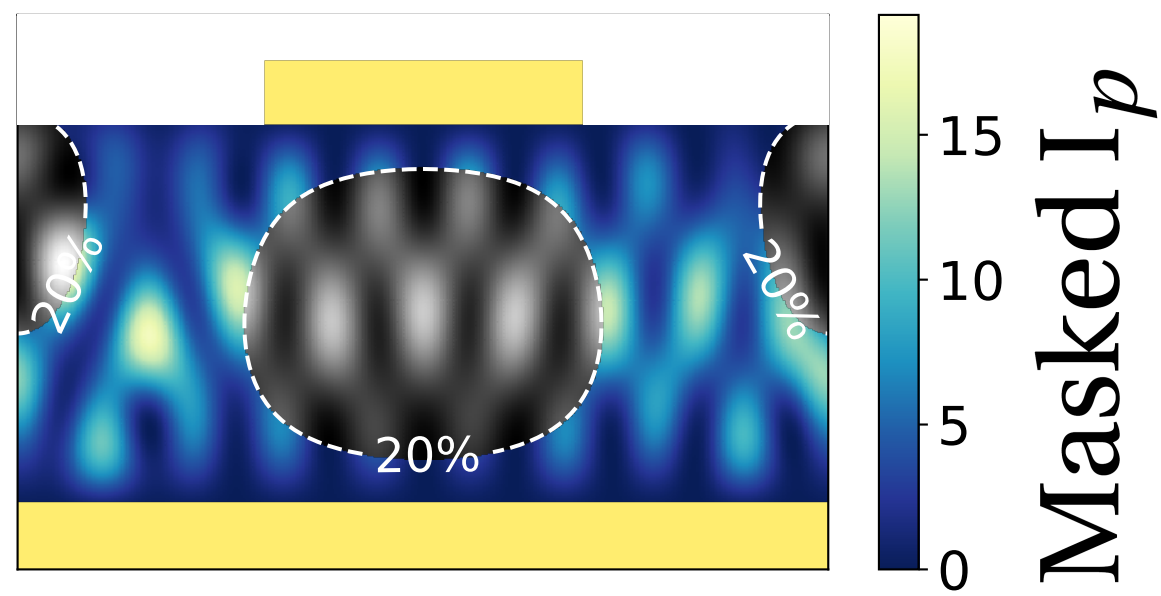
(b)

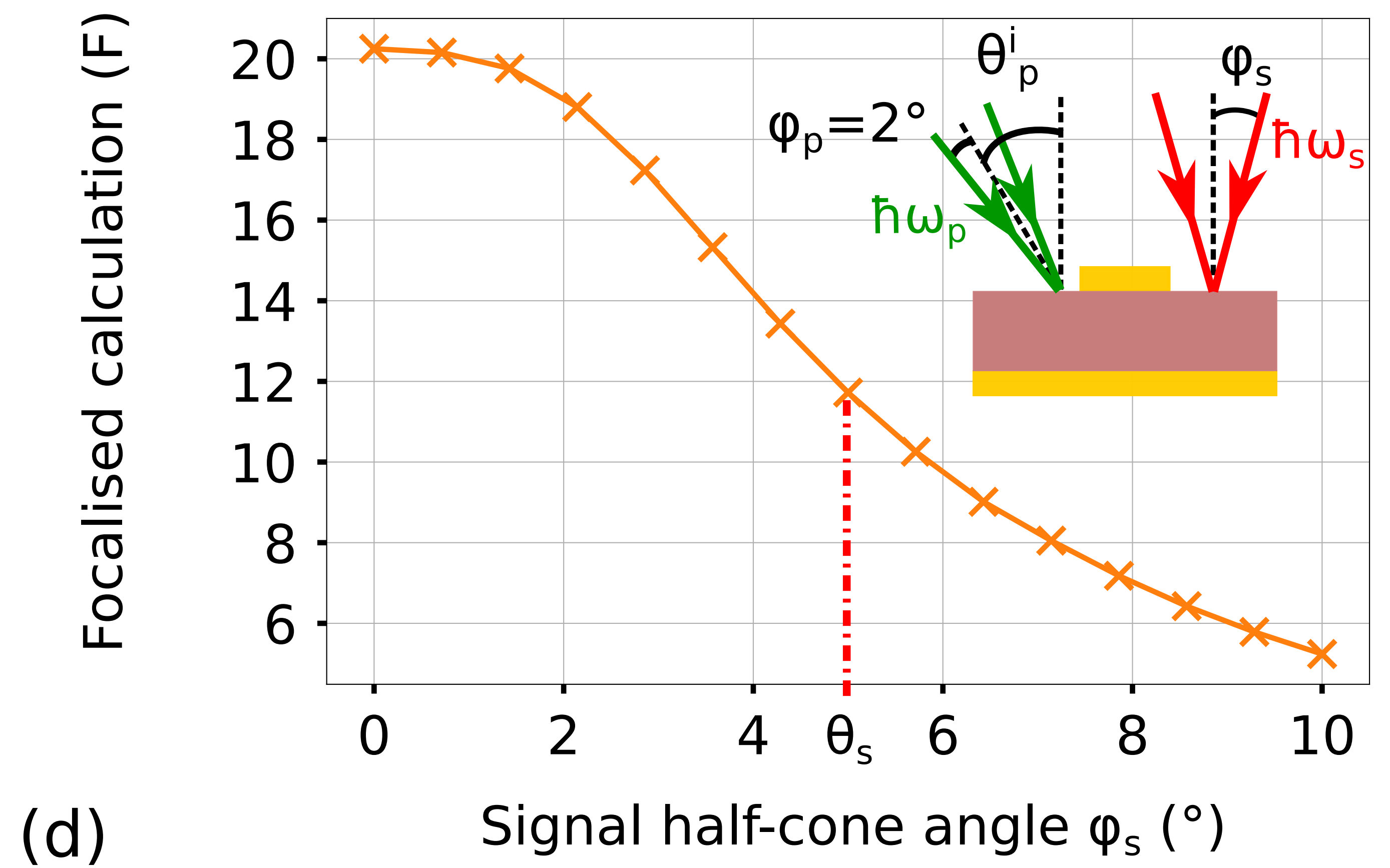
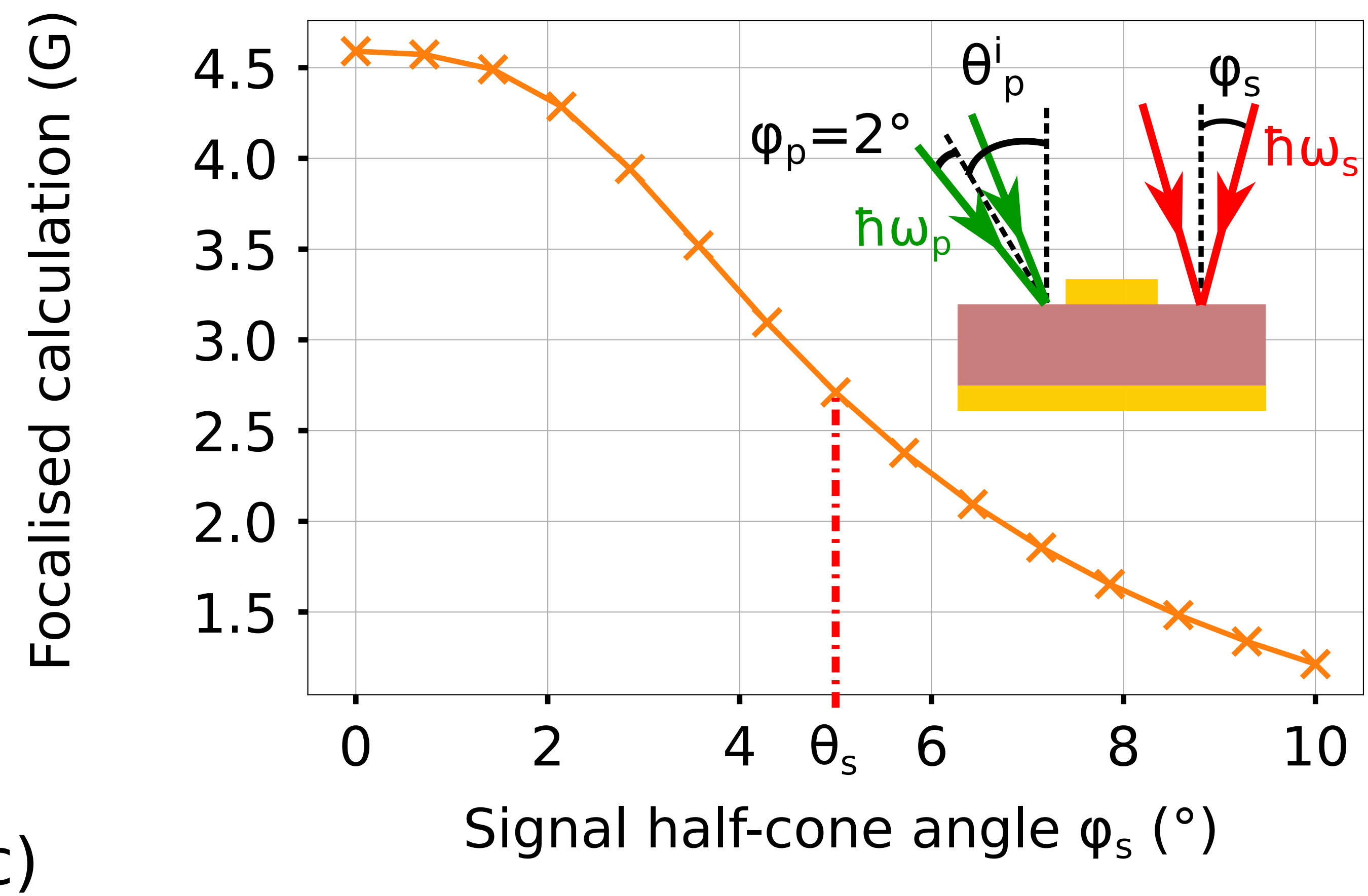
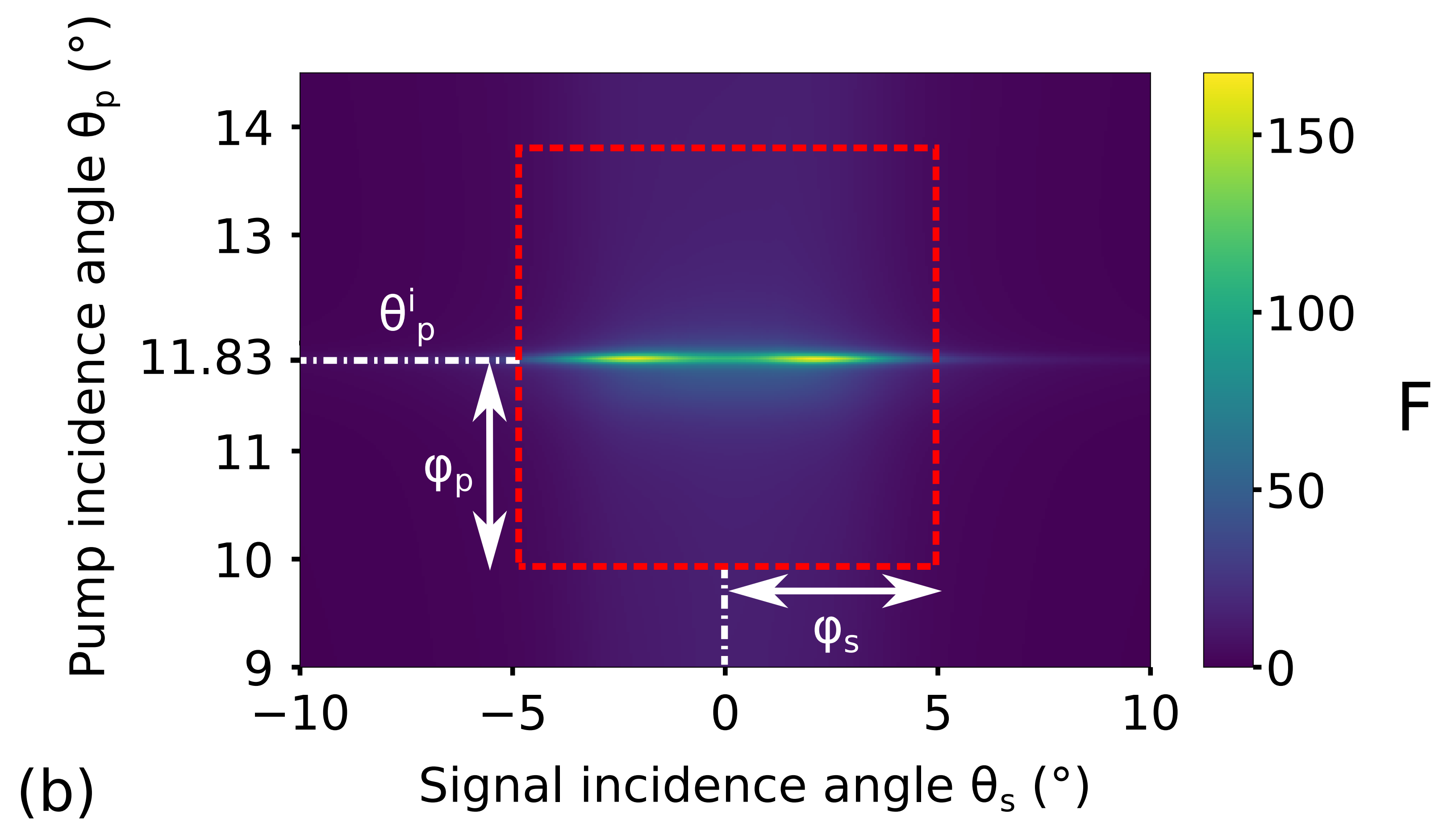
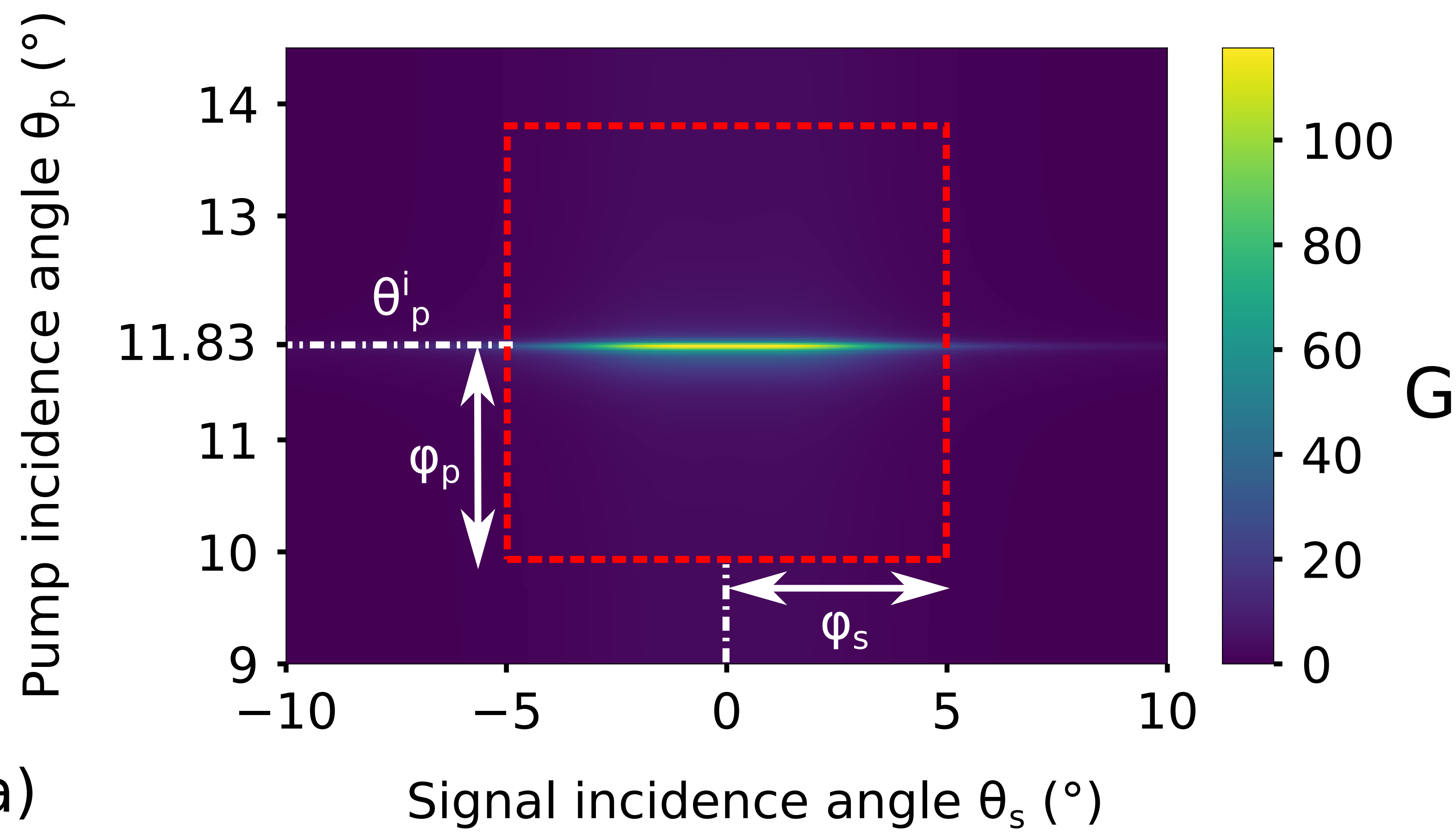


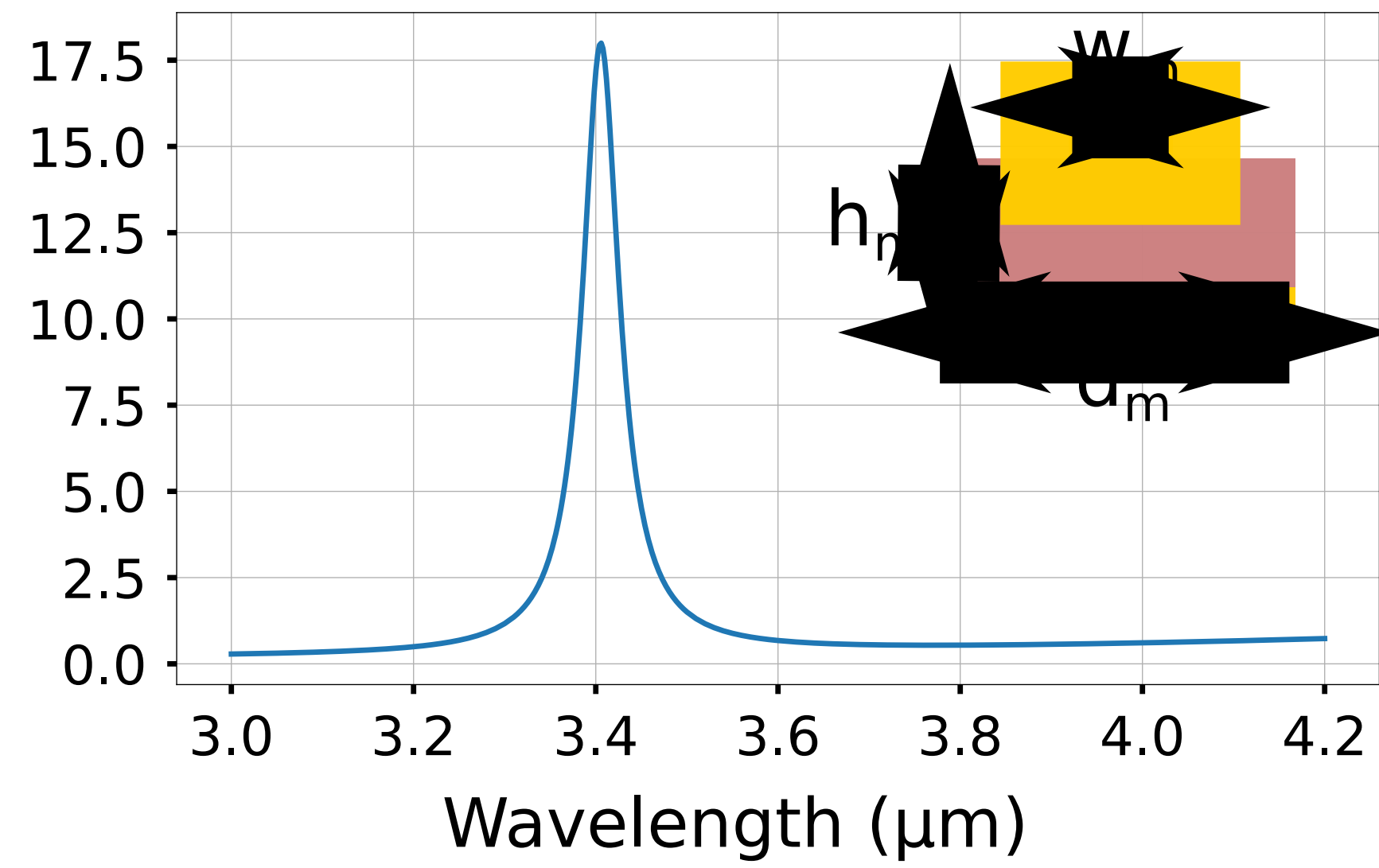
(c)



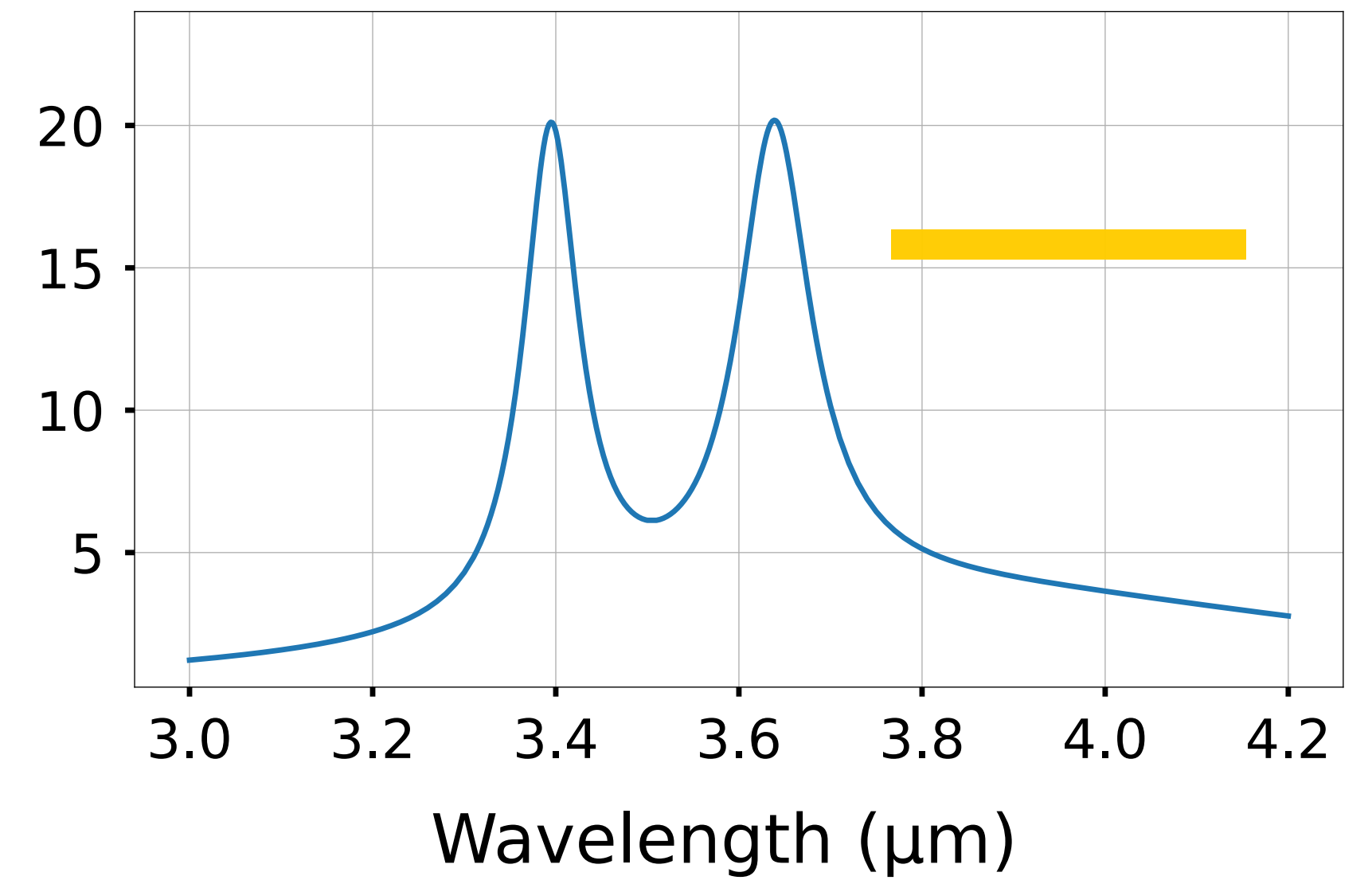
(d)



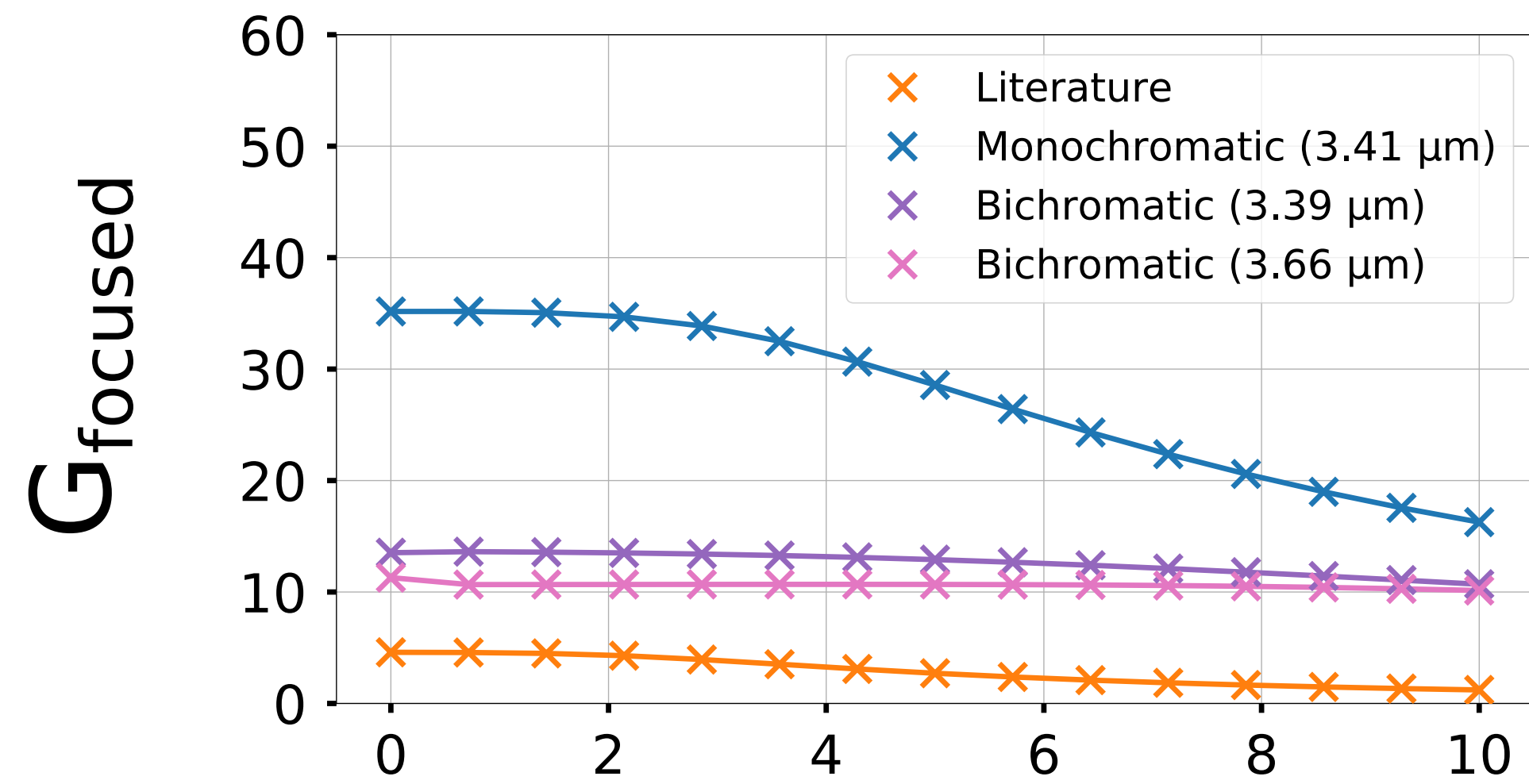




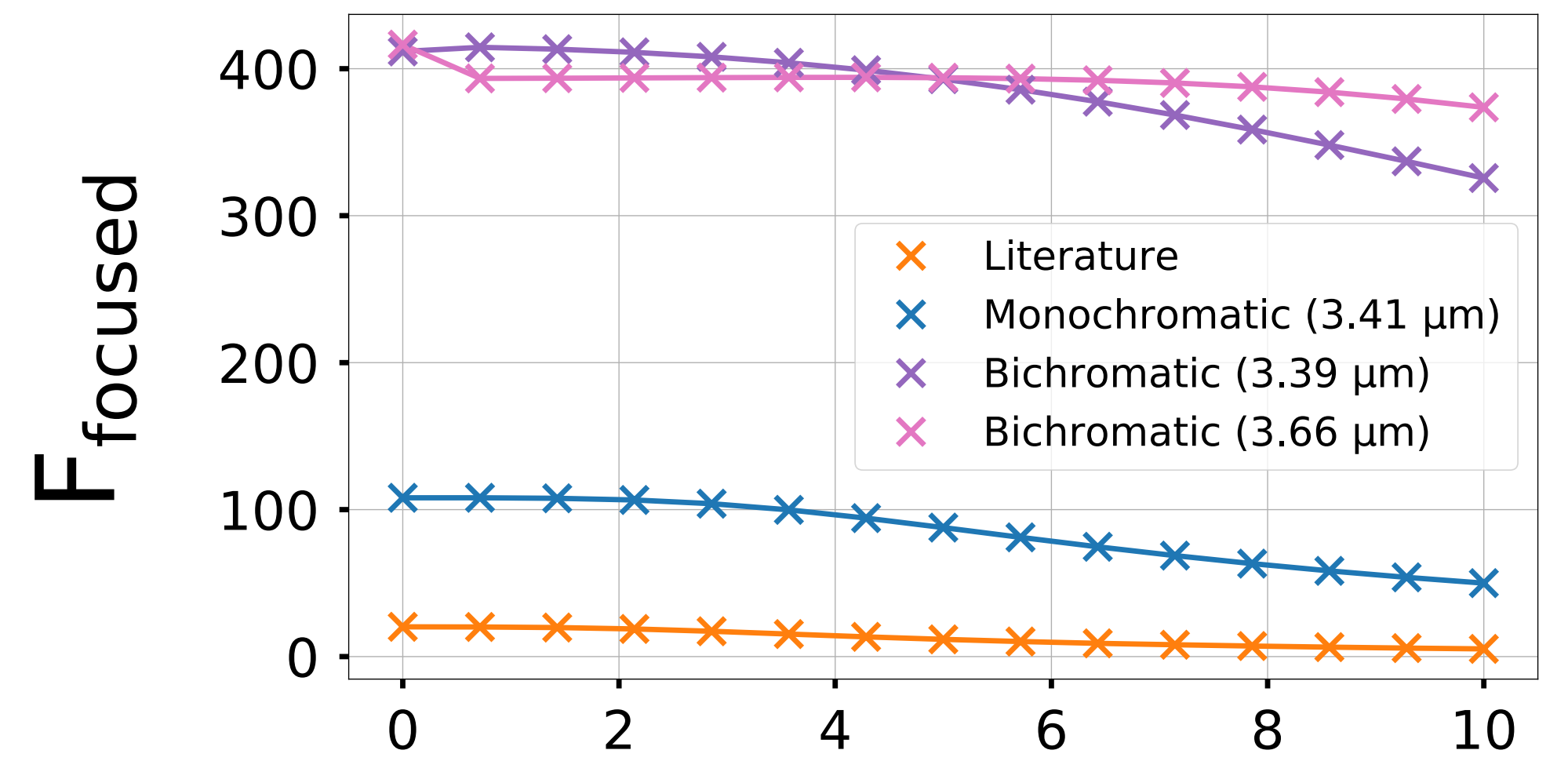
(a)



(b)



(c)



(d)

Supplementary materials

Monochromatic structure

The monochromatic structure depicted is an InP PIN junction absorbing at $3.41 \mu\text{m}$ for monochromatic LIDAR or heterodyne detection.

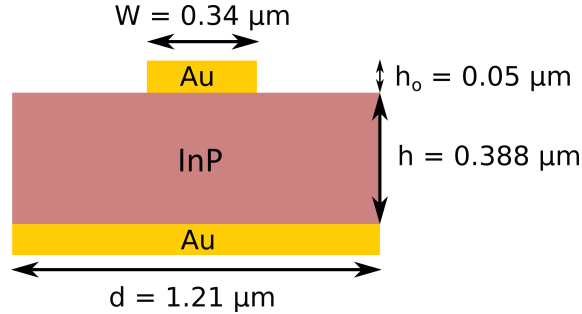


Figure 1: Drawing of the monochromatic nanostructured photodiode.

Intensity maps

The structure has been numerically simulated by the linear B-Spline modal method [1]. All of the intensity maps have been depicted figure 1. These maps are related to the absorption processes that are possible according to the signal and pump interaction. The signal intensity distribution is characteristic from a guided mode, and defines where the NDTPA should happen (figure 2.a). The pump intensity distribution comes from a vertical Fabry-Perot (figure 2.b), but only the area colocalised with the signal activates NDTPA (figure 2.c). The area \mathcal{A} with detrimental pump photons may generate PASRH or DTPA (figure 2.d).

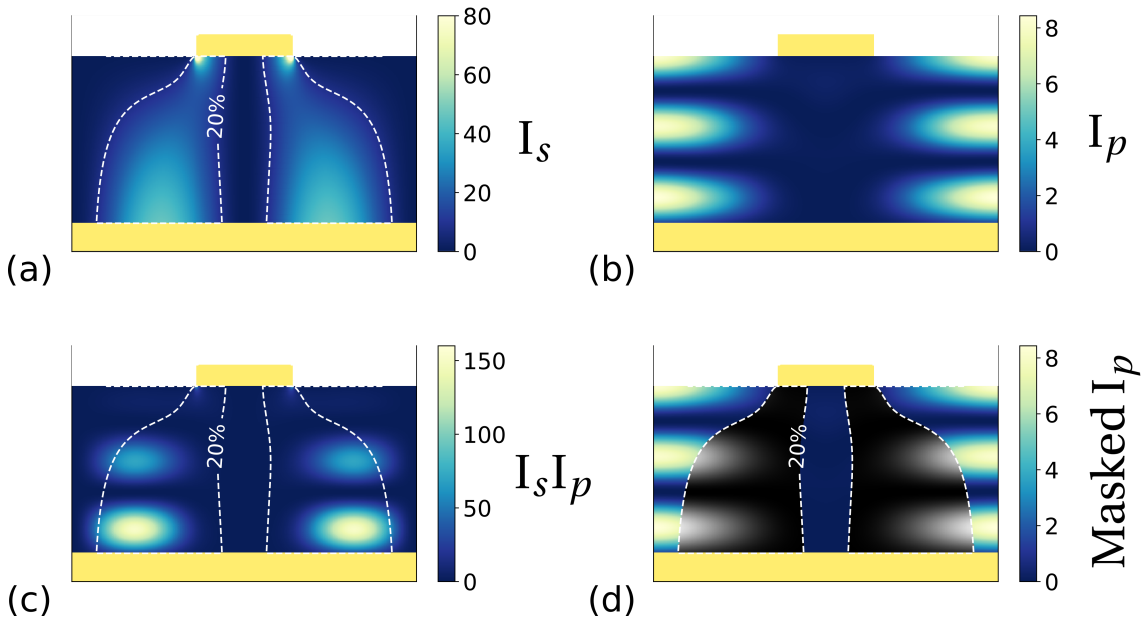


Figure 2: (a). Signal intensity map. A white dotted isoline delimits the surface \mathcal{A} where $I_s < 20\% I_s^{\text{max}}$. (b). Pump intensity map (c). Intensity maps of the signal and pump colocalisation. NDTPA is only generated in this area. (d). Pump intensity map in \mathcal{A} . This pump intensity is detrimental for infrared photodetection through NDTPA.

Figure of merits calculation

The structure figure of merits for collimated beams are depicted figure 3. The gain and FOM evolution are favorable to focused beams due to a great angular tolerance. Only a gain drop around 6° restrains the signal beam aperture.

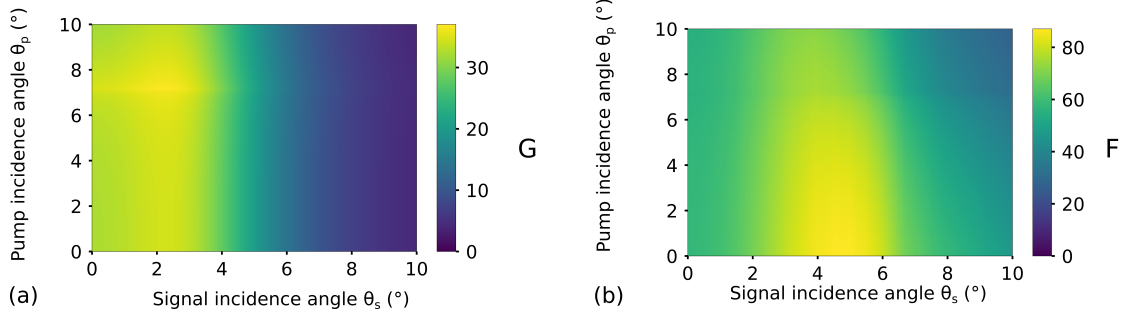


Figure 3: G (a) and F (b) for different incidence signal and pump angles. Both figures depict the best configurations for the detection. The computation were performed for collimated beams.

Bichromatic structure

The bichromatic structure depicted is a GaAs PIN junction absorbing at both 3.39 μm and 3.66 μm for imagery applications.

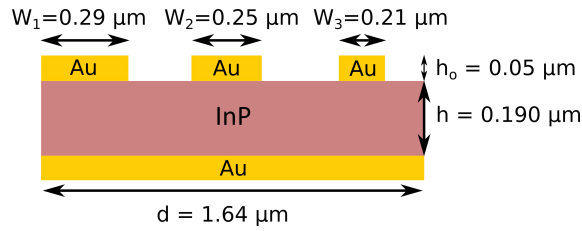


Figure 4: Drawing of the bichromatic nanostructured photodiode.

Intensity maps

Similarly as the previous structure, the intensity maps have been numerically simulated by the linear B-Spline modal method [1] and depicted figure 5. Both signal intensities distributions (3.39 and 3.66 μm) are characteristic from a coupled nano Fabry-Perot resonator [2], and define where the NDTPA should happen (figure 2.a and 2.b). The pump intensity distribution comes from a guided mode resonance (figure 5.c). However, the area colocalised whether with the 3.39 μm signal or 3.66 μm signal distribution is useful to activate NDTPA (figure 2.d and 2.e)). This is taken into account as the surface \mathcal{A} with detrimental pump photons is defined as $\mathcal{A} = \mathcal{A}_{3.39 \mu\text{m}} \cup \mathcal{A}_{3.66 \mu\text{m}}$ (figure 2.f).

Figure of merits calculation

The structure figure of merits for both 3.39 and 3.66 μm collimated beams are depicted respectively figure 6 and figure 7. The gain and FOM evolution are similar for both signals as their distributions come from the same resonator. The structure is favorable to focused beams due to a great signal angular tolerance. Nonetheless, the gain quickly drop around 1° , restraining the pump beam aperture.

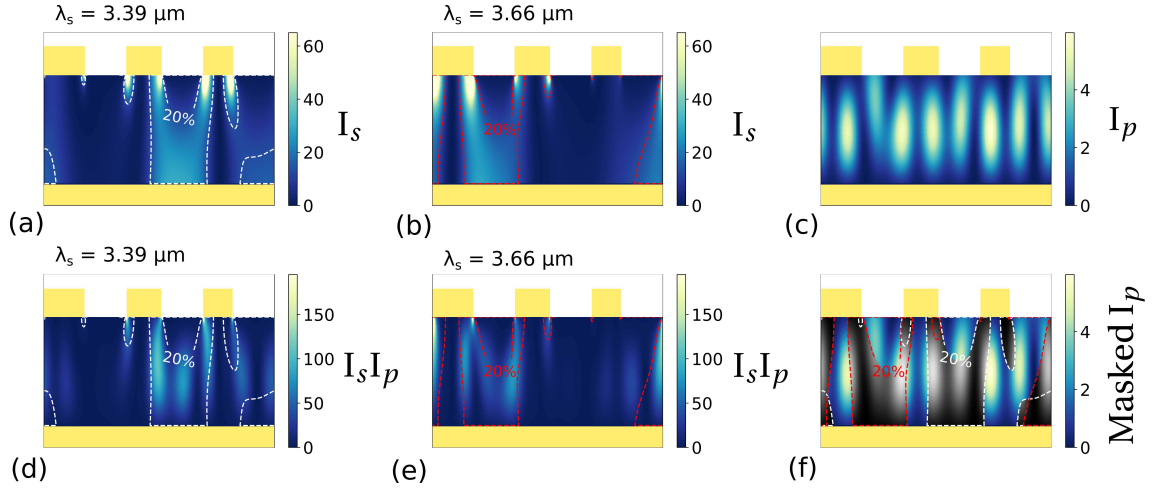


Figure 5: (a). Signal intensity map ($3.39 \mu\text{m}$). A white dotted isoline delimits the surface $\mathcal{A}_{3.39}$ where $I_s < 20\% I_s^{\text{max}}$. (b). Signal intensity map ($3.66 \mu\text{m}$). A red dotted isoline delimits the surface $\mathcal{A}_{3.66}$. (c). Pump intensity map (d). Intensity map of the signal ($3.39 \mu\text{m}$) and pump colocalisation. (e). Intensity map of the signal ($3.66 \mu\text{m}$) and pump colocalisation. (f). Pump intensity map in $\mathcal{A} = \mathcal{A}_{3.39} \cup \mathcal{A}_{3.66}$.

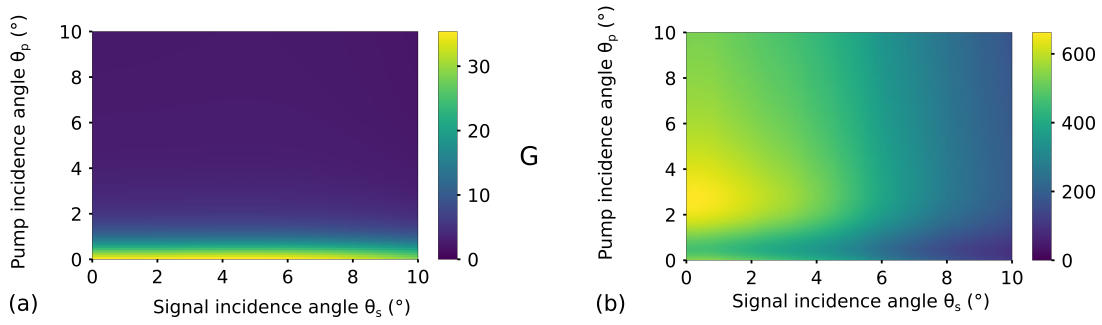


Figure 6: G (a) and F (b) for different incidence signal ($3.39 \mu\text{m}$) and pump ($1.06 \mu\text{m}$) angles. Both figures depict the best configurations for the detection. The calculation were performed for collimated beams.

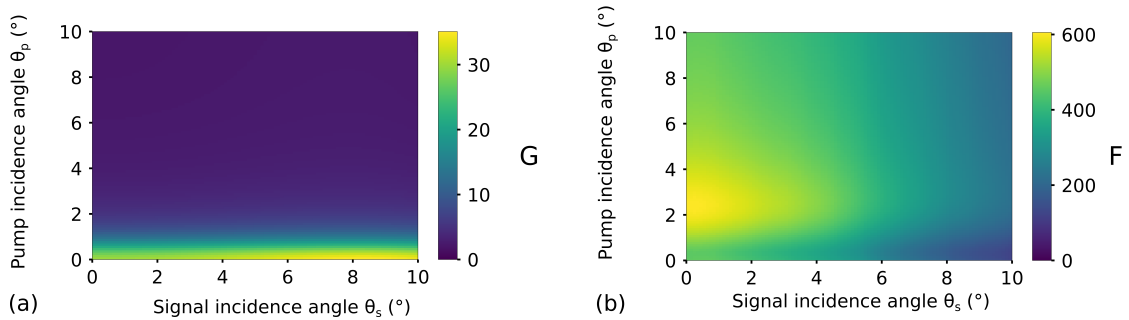


Figure 7: G (a) and F (b) for different incidence signal ($3.66 \mu\text{m}$) and pump ($1.06 \mu\text{m}$) angles. Both figures depict the best configurations for the detection. The calculation were performed for collimated beams.

References

- [1] P. Bouchon, F. Pardo, R. Haïdar, and J.-L. Pelouard, "Fast modal method for subwavelength gratings based on B-spline formulation," *Journal of the Optical Society of America A*, vol. 27, p. 696, Apr. 2010.
- [2] B. Fix, J. Jaeck, P. Bouchon, S. Héron, B. Vest, and R. Haïdar, "High-quality-factor double Fabry-Perot plasmonic nanoresonator," *Optics Letters*, vol. 42, pp. 5062–5065, Dec. 2017. Publisher: Optical Society of America.